Escola de Primavera de Transição e Turbulência
Blumenau 2020

ABCM
Associação Brasileira de Engenharia e Ciências Mecânicas

12th Spring School on Transition and Turbulence
September 21st-25th, 2020, Blumenau, SC, Brazil

EPTT-2020-0003
THE PLUNGING OF HYPERPYCNAL PLUMES ON TILTED BED BY THREE-DIMENSIONAL LARGE-EDDY SIMULATIONS

Felipe Nornberg Schuch
Jorge Hugo Silvestrini
School of Technology, Pontifical Catholic University of Rio Grande do Sul, Porto Alegre, Brazil.
felipe.schuch@edu.pucrs.br, jorgehs@pucrs.br

Eckart Meiburg
Department of Mechanical Engineering, University of California Santa Barbara, Santa Barbara, USA
meiburg@engineering.ucsb.edu

Sylvain Laizet
Department of Aeronautics, Imperial College London, London, SW7 2AZ, UK
s.laizet@imperial.ac.uk

Abstract. *Theoretical and experimental interest in the transport and deposition of sediments from rivers to oceans has increased rapidly over the last two decades. The marine ecosystem is strongly affected by mixing at river mouths, with for instance anthropogenic actions like pollutant spreading. Particle-laden flows entering a lighter ambient fluid (hyperpycnal flows) can plunge at a sufficient depth, and their deposits might preserve a remarkable record across a variety of climatic and tectonic settings. Numerical simulations play an essential role in this context since they provide information on all flow variables for any point of time and space. This work offers valuable Spatio-temporal information generated by turbulence-resolving 3D simulations of poly-disperse hyperpycnal plumes over a tilted bed. The simulations are performed with the high-order flow solver Xcompact3d, which solves the incompressible Navier-Stokes equations on a Cartesian mesh using high-order finite-difference schemes. Five cases are presented, with different values for flow discharge and sediment concentration at the inlet. A detailed comparison with experimental data and analytical models is already available in the literature. The main objective of this work is to present a new data-set that shows the entire three-dimensional Spatio-temporal evolution of the plunge phenomenon and all the relevant quantities of interest.*

Keywords: *Turbidity Current, Plunging Flow, Computational Fluid Dynamics, Large-Eddy Simulation, Xcompact3d.*

1. INTRODUCTION

Hyperpycnal plumes are produced when the density of a fluid entering in a quiescent basin is higher than that in the ambient fluid. They are observed in nature when a river transports enough suspended sediment to be denser than the environment where it flows into, such as channels, lakes, reservoirs or the ocean (Mulder *et al.*, 2003; Lamb and Mohrig, 2009). When the inflow momentum decreases, it eventually plunges under the ambient fluid and flows along the bed as an underflow density current, as illustrated in Fig. 1. The inflow can be characterized by its initial depth $\tilde{h}_0$ (where $\tilde{\ }$ corresponds to dimensional quantities), volumetric discharge per unit width $\tilde{Q}_0$ and fresh water density plus an excess due to suspended sediments $\tilde{\rho}_w + \Delta\tilde{\rho}$. The plunging of the hyperpycnal flow can be represented by three main regions. The depth-limited plume is a homogeneous flow region that occupies the complete channel depth, and it is dominated by inertial forces. At sufficient depth $\tilde{H}_p$, the flow collapses in the so-called plunge region. Downstream, a turbidity current is formed, dominated by buoyancy forces, and can be characterized by new values of depth $\tilde{H}_d$, discharge $\tilde{Q}_d$ and density $\tilde{\rho}_a + \Delta\tilde{\rho}_d$, due to continuous mixing between ambient fluid and the underflow (García, 1996). Many authors express this increase in flow discharge through the incorporation of ambient fluid in the form of the initial mixture coefficient $\gamma = \tilde{Q}_d/\tilde{Q}_0 - 1$.

The understanding of the parameters and mechanisms that govern the flow transition in the plunge zone is relevant in terms of the health of ecosystems in river deltas regions (Horner-Devine *et al.*, 2015), in the management and operation of dam reservoirs (Chamoun *et al.*, 2016) and in the field of geology, since old sand deposits can preserve records of climatic and tectonic environments (Mulder *et al.*, 2003), in addition to becoming important hydrocarbon reservoirs (Meiburg and Kneller, 2010). Many studies about this flow configuration are becoming available in the literature, including field observations (Wunderlich and Elder, 1973; Ford and Johnson, 1981; Best *et al.*, 2005), analytical models (Akiyama and
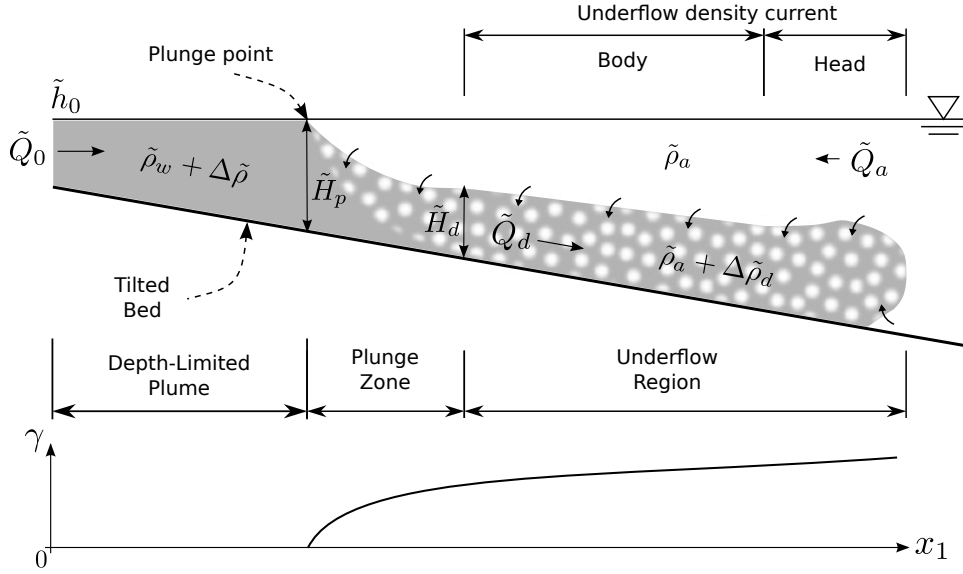
Figure 1. Illustration of the plunging of an hyperpynal flow in a tilted channel. The mixing coefficient $\gamma = \tilde{Q}_d/\tilde{Q}_0 - 1$ is represented for reference. Source: Modified from Schuch *et al.* (2018).

Stefan, 1984; Parker and Toniolo, 2007; Dai and García, 2009), experiments (Singh and Shah, 1971; Arita and Nakai, 2008; Lamb *et al.*, 2010) and numerical simulations (Farrell and Stefan, 1986; Kassem and Imran, 2001; Dai *et al.*, 2007). In this context, numerical simulations unlike field observations and experiments, can play an important role since they can provide information for all flow variables at any point in time and space. Schuch *et al.* (2018) presented a new numerical framework for the reproduction and analysis of the plunge phenomenon and its associated flow features, where the results of the three-dimensional turbulence-resolving simulations were compared with experimental data (Lamb *et al.*, 2010) and analytical models (Parker and Toniolo, 2007), and good agreement was found between them.

The main objective of this work is to present an original data-set that registers the entire Spatio-temporal evolution of the plunge phenomenon and all relevant quantities. To generate this new data-set, the numerical methodology proposed by Schuch *et al.* (2018) was slightly modified, the simulated time is extended by 20%, the computational domain is six times wider and the flow variables are considered in a layer averaged context. Additionally, the spatial-temporal data is available online[1], in order to support future research.

2. METHODOLOGY

For the present study, N transport equations under the Boussinesq approximation can be used, in addition to the incompressible Navier-Stokes equations. They are written in their dimensionless form as

$$\frac{\partial u_j}{\partial x_j} = 0, \tag{1a}$$

$$\frac{\partial u_i}{\partial t} = -u_j \frac{\partial u_i}{\partial x_j} - \frac{\partial p}{\partial x_i} + \frac{1}{Re} \frac{\partial^2 u_i}{\partial x_j \partial x_j} + e_i^g \frac{1}{Fr_0^2} \sum_{\ell=1}^{N} c_\ell, \tag{1b}$$

$$\frac{\partial c_\ell}{\partial t} = -\left(u_j + u_{s,\ell} e_j^g\right) \frac{\partial c_\ell}{\partial x_j} + \frac{1}{ReSc} \frac{\partial^2 c_\ell}{\partial x_j \partial x_j}, \quad \ell = 1, \dots, N, \tag{1c}$$

where u_i, p and c correspond to velocity, pressure and suspended particle concentration, respectively, together with the coordinate system x_i (see Figure 2), time t, unit vector pointing in gravity direction $e^g = [0,1,0]$ and the particle's settling velocity u_s. It is related to the particle diameter by the Stokes settling velocity law (Julien, 1998) which assumes that the dominant flow force on an individual particle is the Stokes drag. The Reynolds, Schmidt and initial densimetric Froude numbers at the inlet, besides the Stokes settling velocity are the four dimensionless parameters that describe the problem, they are defined as follow

---

[1] https://github.com/fschuch/the-plunging-flow-by-3D-LES

$$Re = \frac{\tilde{Q}_0}{\tilde{\nu}}, \tag{2a}$$

$$Sc_\ell = \frac{\tilde{\nu}}{\tilde{D}_\ell}, \quad \ell = 1, \dots, N, \tag{2b}$$

$$Fr_0 = \frac{\tilde{Q}_0^2}{\sqrt{R\tilde{C}_0 \tilde{g}\tilde{h}^3}}, \tag{2c}$$

$$u_{s,\ell} = \frac{\tilde{u}_{s,\ell} \tilde{h}_0}{\tilde{Q}_0} = \frac{\tilde{d}_{s,\ell}^2 R\tilde{g}\tilde{h}_0}{18\tilde{\nu}\tilde{Q}_0}, \quad \ell = 1, \dots, N, \tag{2d}$$

where $\tilde{Q}_0$ and $\tilde{C}_0$ are the volumetric discharge per unit width and volumetric sediment concentration at the inlet of the channel. The kinematic viscosity is $\tilde{\nu}$, the fresh water and sediment densities are $\tilde{\rho}_w$, $\tilde{\rho}_s$, with R defined as $(\tilde{\rho}_s - \tilde{\rho}_w)/\tilde{\rho}_w$. The gravity acceleration is $\tilde{g}$, the diffusivity of particle concentration is $\tilde{D}$ and the grain size is $\tilde{d}_s$. All parameters and variables are made dimensionless using the influx velocity $\tilde{U}_0$, depth $\tilde{h}_0$ and sediment concentration $\tilde{C}_0$.

The computational setup (see Fig. 2) is based on the experimental channel configuration of Lamb *et al.* (2010) and the numerical study of Schuch *et al.* (2018). The test section (TS) is the region where the flow is analyzed, whose dimensions are $(L_1, L_2, L_3) = (250.0h_0, 16.875h_0, 24.0h_0)$. Notice that the dimensionless initial depth is $h_0 = 1$. The bed slope $S = 5\%$ is included in the computational domain via an immersed boundary method (IBM), following the alternating direction forcing strategy proposed by Gautier *et al.* (2014). Two sponge zones are employed for different reasons. Firstly, SZ_a provides the particle-laden flow upstream of the test section, with a recycling technique in order to generate a turbulent inflow condition. Secondly, SZ_b applies an intrinsic profile for the stream-wise velocity u_1 near the outflow boundary, in order to reduce the turbulence level to zero. The horizontal extension of the sponge zones are $(L_{1a}, L_{1b}) = (25.0, 62.5)$. The entire computational domain is discretized using $(n_1, n_2, n_3) = (1081, 121, 90)$ mesh points. A time step of $\Delta t = 0.0125$ is employed for a total of 4.8×10^5 iterations. In comparison with the previous study of Schuch *et al.* (2018), the numerical channel in this study is now six times wider, in a dimension compatible with the experimental reference if an initial depth of $\tilde{h}_0 = 10\ mm$ is considered, and the simulated time is extended from 5,000 to 6,000 dimensionless units, an increasing of 20%. A nondeformable water surface is imposed as top boundary condition (where $x_2 = 0$), which is described by Nasr-Azadani *et al.* (2013) as a free-slip condition for velocity and no-flux condition for the concentration field. The bottom boundary condition (at the solid/fluid interface) is no-slip for velocity and one-dimensional convective outflow for concentration, as functions of the settling velocity u_s (Necker *et al.*, 2002). Inflow and outflow conditions are handled by both sponges zones and periodic boundary condition is employed in the spanwise direction (x_3). For the initial condition, the domain is filled with freshwater at rest ($u_i = c_\ell = 0$). For more details about the computational setup see Schuch (2020).
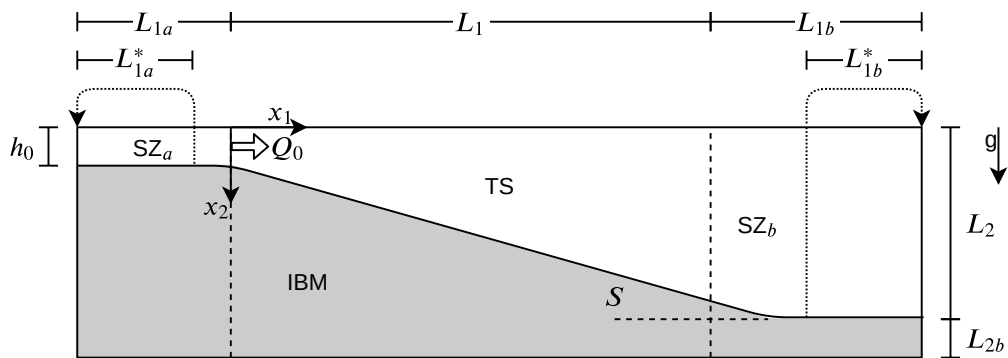

Figure 2. Schematic representation of the computational domain (not to scale). Spanwise coordinate x_3 is perpendicular to the plane. In gray, the tilted bed is inserted by immersed Boundary Method (IBM); TS represents the test section, where the flow is analyzed; SZ_a and SZ_b represent the sponge zones. Source: Modified from Schuch (2020).

The numerical simulations were carried out by the high-order Navier-Stokes solver `Xcompact3d`[2], an open source tool based on the Boussinesq system for incompressible fluids, designed for High Performance Computing (Laizet and Lamballais, 2009; Laizet and Li, 2011; Bartholomew *et al.*, 2020). The governing equations (1) are solved under an implicit Large-Eddy Simulations approach, in which only the largest and energy-containing flow structures are resolved.

---

[2]The code is available at https://github.com/xcompact3d/Incompact3d.

Table 1. Volumetric discharge per unit width $\tilde{Q}_0$ and volumetric sediment concentration $\tilde{C}_0$ recorded at the inlet from the experiments of Lamb *et al.* (2010), in addition to the respective Reynolds number Re, initial densimetric Froude number Fr_0 and Stokes settling velocity $u_{s,\ell}$ for each granulometric fraction. Source: Modified from Lamb *et al.* (2010).

Simulations	2	4	5	6	7
$\tilde{Q}_0 (m^2/s)$	0.0043	0.0025	0.0033	0.0043	0.0043
$\tilde{C}_0 (\%)$	0.36	0.54	0.54	0.54	1.00
Re	4,300	2,500	3,300	4,300	4,300
Fr_0	17.81	8.45	11.16	14.54	10.68
$u_{s,1} \times 10^{-5}$	1.9	3.2	2.5	1.9	1.9
$u_{s,2} \times 10^{-3}$	0.9	1.6	1.2	0.9	0.9
$u_{s,3} \times 10^{-3}$	3.9	6.7	5.0	3.9	3.9

On the other hand, the small scales are not resolved, instead, they are modeled via an artificial dissipation that takes place when computing the viscous term (Sagaut, 2006; Grinstein *et al.*, 2007; Lamballais *et al.*, 2011; Dairay *et al.*, 2017).

Seven experiments were carried out by Lamb *et al.* (2010), and five of them are reproduced in this study, as shown in Tab. 1. The experimental grain-size distribution (crushed silica $\tilde{\rho}_s = 2,650\ kg/m^3$) is modelled by three diameters ($\tilde{d}_{s,1} = 3\ \mu m$, $\tilde{d}_{s,2} = 21\ \mu m$ and $\tilde{d}_{s,3} = 43\ \mu m$) in a distribution of about one third for each grain size. The Schmidt number Sc is equal to 1 in the present study. Notice that cases 2, 6 and 7 have the same flow discharge $\tilde{Q}_0$ and increasing sediment concentration $\tilde{C}_0$, while cases 4, 5 and 6 have the same sediment concentration $\tilde{C}_0$ and increasing flow discharge $\tilde{Q}_0$. The validation of the numerical framework employed here for the problem illustrated in Fig. 1 is out of the scope of this study, since a complete comparison between numerical, experimental and analytical models is already available at Schuch *et al.* (2018).
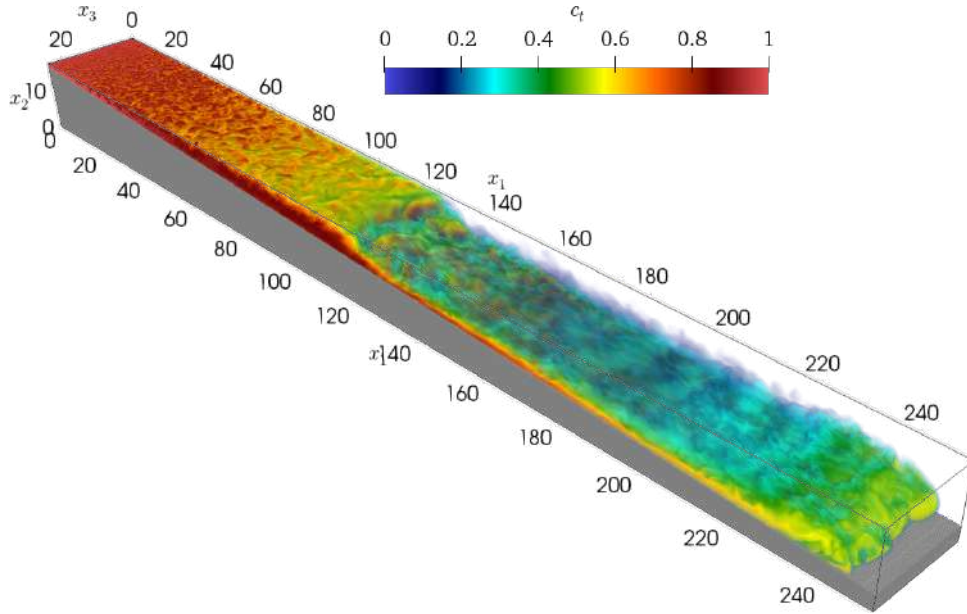
3. RESULTS

Figure 3. Instantaneous volumetric visualization of the total concentration field c_t for case 4 at $t = 1,000$.

A sample of the tridimensional plunging flow is shown in Fig. 3, represented by a snapshot of the total concentration field ($c_t = c_1 + c_2 + c_3$) for case 4 at dimensionless time equals to $t = 1,000$. In this figure, the plunge line is visible near $x_1 = 120$, as well as the body and head of the underflow turbidity current downstream plunging, including the lobes and clefts structures at the front. The dimensionless total concentration is one (red color) right at the inlet of the test section, and then decays due to sedimentation with the stream-wise coordinate x_1. Besides that, the turbulent mixing between the turbidity current and the ambient fluid is evidenced by the dark blue color, which corresponds to low concentration levels.

The complete spatio-temporal analysis of the relevant quantities is possible in a layer averaged context per width unit,
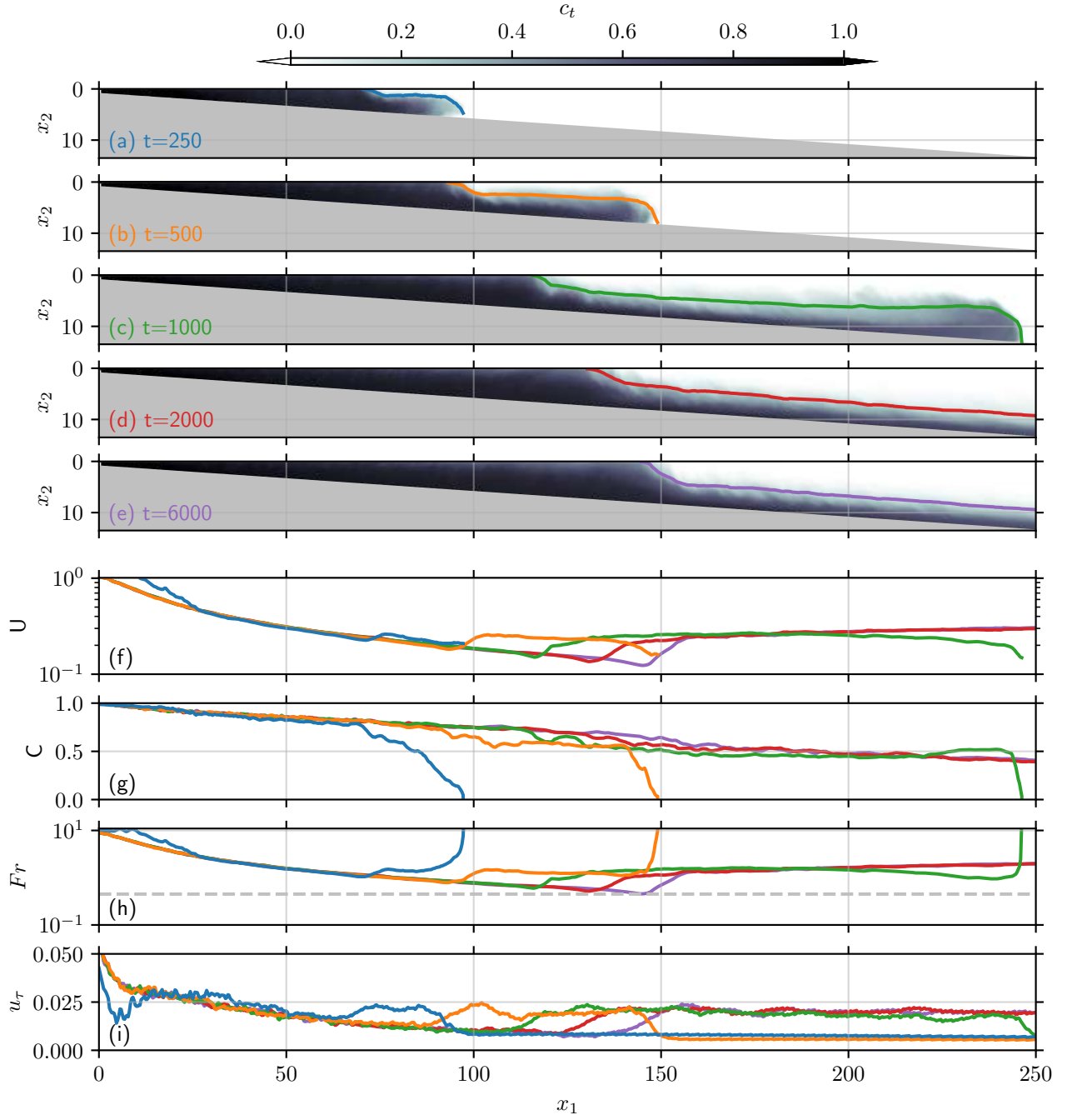
Figure 4. Case 4 spanwise-averaged total concentration field c_t for dimensionless time equals to 250, 500, 1,000, 2,000 and 6,000 from (a) to (e), respectively. In addition to layer-averaged flow depth H (colored lines from a to e), streamwise velocity U (f), concentration C (g) and local densimetric Froude number Fr (h), $Fr_p = 0.45$ is shown in dashed line for reference, computed according to Eq. (4), besides the spanwise-averaged bed shear velocity u_τ (i), expressed by Eq. (5).

that is computed following Ellison and Turner (1959) according to the equations

$$Uh(x_1,t) = \frac{1}{L_3} \int_0^{L_3} \int_{x_{2r}}^{x_{2i}} u_1(x_1,x_2,x_3,t)\, dx_2 dx_3, \tag{3a}$$

$$U^2 h(x_1,t) = \frac{1}{L_3} \int_0^{L_3} \int_{x_{2r}}^{x_{2i}} \left(u_1(x_1,x_2,x_3,t)\right)^2 dx_2 dx_3, \tag{3b}$$

$$UCh(x_1,t) = \frac{1}{L_3} \int_0^{L_3} \int_{x_{2r}}^{x_{2i}} u_1(x_1,x_2,x_3,t)\, c_t(x_1,x_2,x_3,t)\, dx_2 dx_3. \tag{3c}$$

For the vertical integration, x_{2r} represents the bed position and x_{2i} represents the interface between the underflow turbidity current and the ambient fluid, considered in this work as the position where $u_1 \times c_t = 0.005$. Finally, the layer-averaged velocity U, flow depth H, flow discharge Q, concentration C and local densimetric Froude number Fr are obtained respectively as

$$U(x_1,t) = U^2h/Uh, \tag{4a}$$

$$H(x_1,t) = (Uh)^2/U^2h, \tag{4b}$$

$$Q(x_1,t) = Uh, \tag{4c}$$

$$C(x_1,t) = UCh/Uh, \tag{4d}$$

$$Fr(x_1,t) = \frac{Q(x_1,t)}{\sqrt{C(x_1,t)\left(H(x_1,t)\right)^3}}\, Fr_0. \tag{4e}$$

The spatio-temporal evolution of the quantities described above for case 4 are shown in Fig. 4, in addition to the spanwise-averaged total concentration field c_t for dimensionless time equals to 250, 500, 1,000, 2,000 and 6,000, from (a) to (e), respectively. All the features of the plunging flow in a tilted bed (see Fig. 1) can be seen. The plunge point is visible since early times (a and b) and moves downstream, for more advanced time (e) it tends to a quasi-stationary position at around $x_1 = 150$, the same position found experimentally in Lamb *et al.* (2010). Upstream plunging is located the depth-limited flow region, where the inflowing turbidity current has enough momentum to push the ambient fluid downstream. Due to the tilted bed, the flow's depth increases with the streamwise coordinate (x_1) and progressively reduces its velocity until a critical point, the plunge zone, where the flow collapses, accelerates and turns into a density current, governed now by the buoyance forces. This behavior reflects on the layer-averaged velocity U (f), where the maximum value is noticeable at the inflow boundary ($x_1 = 0$) and decreases until its minimum value at the plunge point, where the flow accelerates. Besides that, the incorporation of ambient fluid into the submerged turbidity current (entrainment) increases the flow velocity downstream plunging. The layer-averaged concentration C (g) decays with x_1 due to the sedimentation, and the mixing with the ambient fluid reduces concentration iven more downstream plunging. Besides that, C works as an indicator for the temporal evolution of the front position x_f, which is obtained as the highest value of x_1 where the concentration is non-zero. The densimetric Froude number Fr (h) expresses the ratio between inertial and buoyance forces, that are dominant upstream and downstream plunging, respectively. In this way, Fr is directly related to the stable plunge position, in fact, the Froude value at plunge point observed in Fig. 4h is very close to $Fr_p = 0.45$, a value reported in previous works (Parker and Toniolo, 2007; Lamb *et al.*, 2010; Schuch *et al.*, 2018). The densimetric Froude number is also used to track the temporal evolution of the plunge point position x_p, since it is observed at the absolute minimum value for Fr.

If the flow is sufficiently intense, the turbidity currents can resuspend part of the material previously deposited, or even erode the bed over which it flows, as commented by Necker *et al.* (2002). Even though the numerical configuration of this work does not consider resuspension, a further analysis based on the simulated data can indicate places where the flow is more likely to present such phenomena. For that, the bed shear velocity u_τ has a fundamental role, and can be calculated according to the equation

$$u_\tau = \sqrt{\tau_w}, \quad \text{with} \quad \tau_w = \frac{1}{Re}\sqrt{\left(\frac{\partial \hat{u}_1}{\partial \hat{x}_2}\right)^2 + \left(\frac{\partial \hat{u}_3}{\partial \hat{x}_2}\right)^2}\Bigg|_{x_2 = x_{2i}}. \tag{5}$$

The notation $(\hat{\cdot})$ represents a rotation in the coordinate system, so that $\hat{x}_1$ still points in the preferred flow direction, but is now parallel to the bed, and $\hat{x}_2$ is normal to the bed, while x_{2i} corresponds to the position of the solid-fluid interface. In this way, the velocities required for the calculation are given by

$$\hat{u}_1 = \cos(\theta)u_1 - \sin(\theta)u_2, \tag{6a}$$

$$\hat{u}_3 = u_3, \tag{6b}$$

while the derivative normal to the bed is computed as

$$\frac{\partial}{\partial \hat{x}_2} = \sin(\theta)\frac{\partial}{\partial x_1} + \cos(\theta)\frac{\partial}{\partial x_2}. \tag{7}$$

The bed shear velocity u_τ can be observed in Fig. 4i. It has a behavior very similar to that observed for the layer-averaged velocity U, being maximum at the entrance of the channel an then decreases. The minimum value for u_τ is reached exactly where the reduction in flow's depth occurs, seen solid lines from (a) to (e), there is a local maximum immediately at the plunge point, where Fr is minimum, and then the value stabilizes in the body region, being slightly larger at the
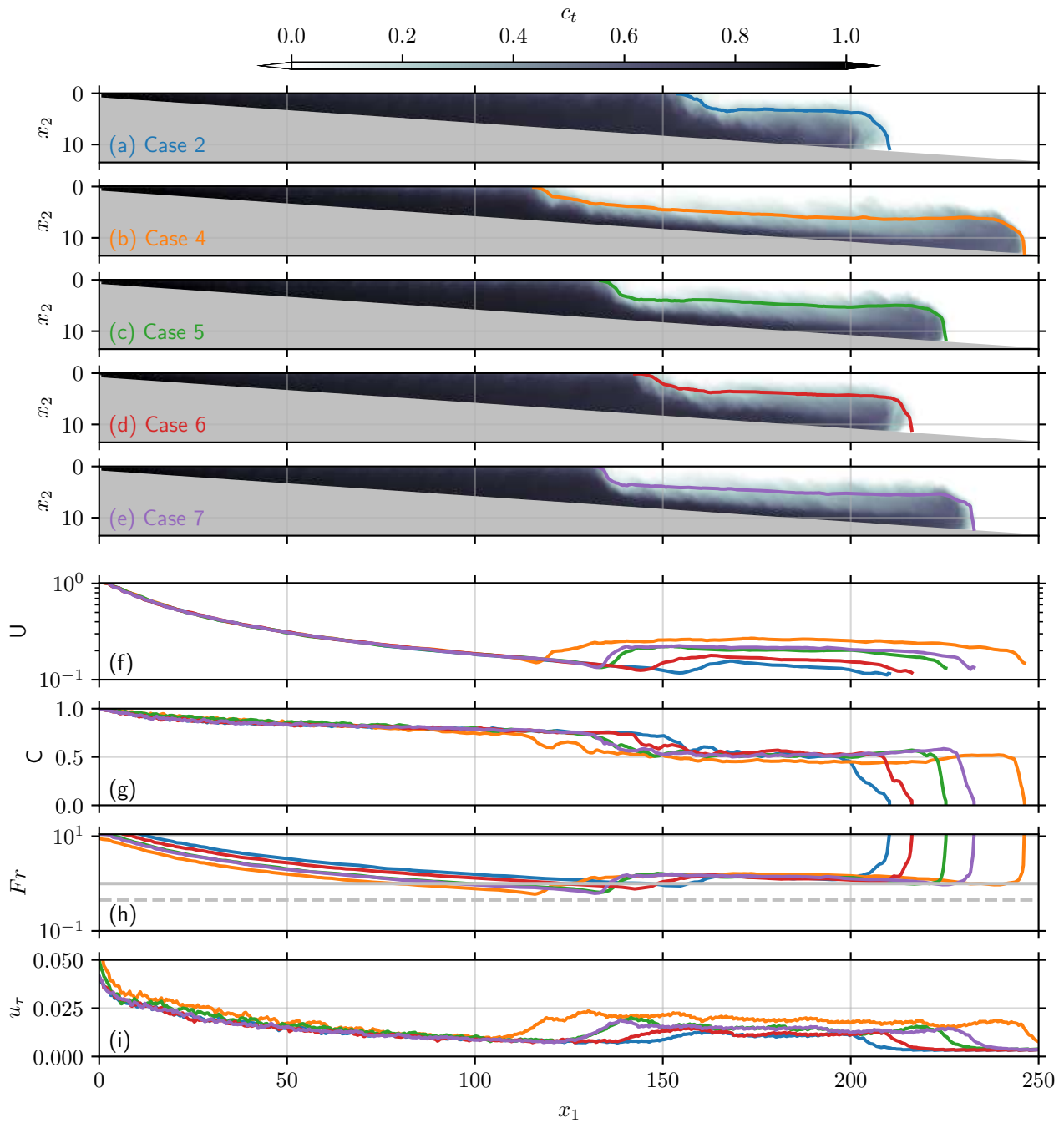
Figure 5. Spanwise-averaged total concentration field c_t for all cases from (a) to (e) at $t = 1,000$. In addition to layer-averaged flow depth H (colored lines from a to e), streamwise velocity U (f), concentration C (g) and local densimetric Froude number Fr (h), 1.0 and 0.45 are shown in solid and dashed lines for reference, computed according to Eq. (4), besides the spanwise-averaged bed shear velocity u_τ (i), expressed by Eq. (5).

head. It indicates that the channel's entrance is the region with the greatest erosive potential, followed by the plunging point and then the head of the turbidity current.

The spanwise-averaged total concentration field c_t for all cases at dimensionless time $t = 1,000$ is shown in Fig. 5, from (a) to (e). Both flow head and plunging zone are well defined for all cases, however, their position is affected by the parameters of each case. In comparison, a plunging upstream accelerates the turbidity current earlier and impulses its body and head, as shown in the layer-averaged velocity U (f). The layer-averaged concentration C (g) is very similar for all cases upstream plunging, however, the value downstream differs due to differences in flow depth and mixing with the ambient fluid. The densimetric Froude number Fr is shown in Fig. 5h. At $t = 1,000$ the plunging for all cases is still in
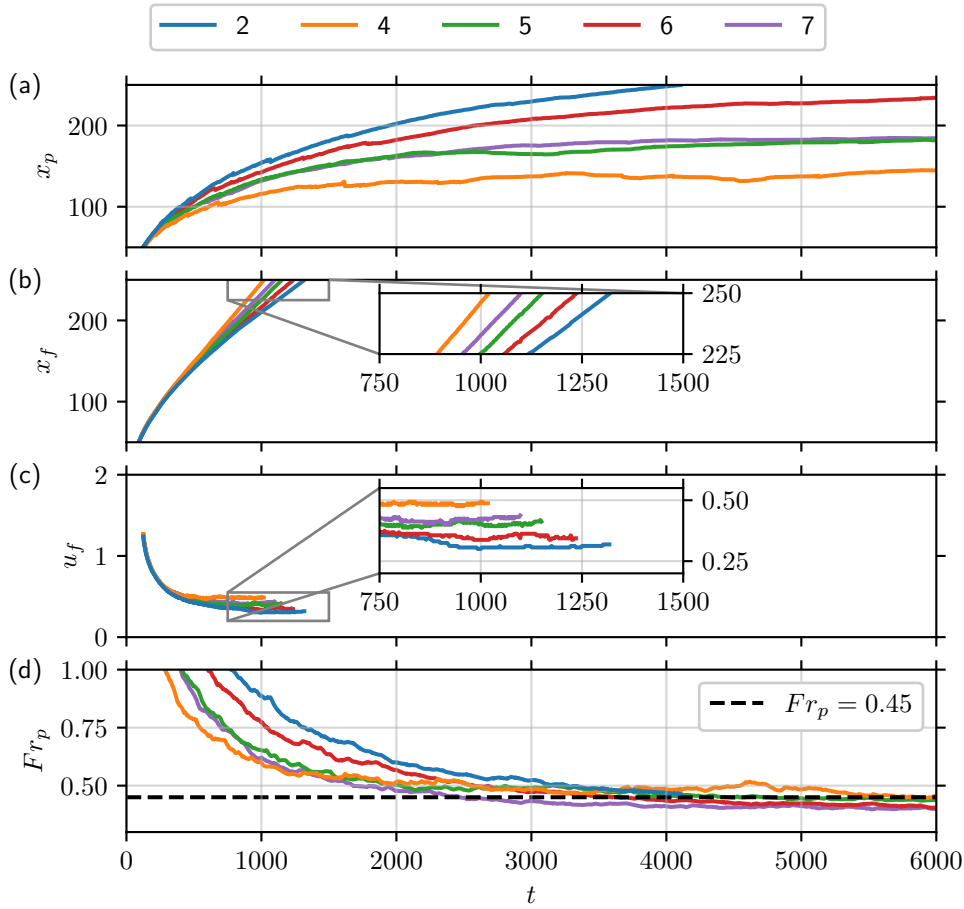
Figure 6. Time evolution of: (a) Distance for plunging x_p, (b) front position x_f, (c) front velocity u_f and (d) densimetric Froude number at plunging point Fr_p, where $Fr_p = 0.45$ is shown for reference.

the transient phase, so the Froude value observed at plunge point is higher than the reference of $Fr_p = 0.45$, on the other hand, the Fr value measured at underflow's head of around an unity is in agreement with previous studies (Sequeiros, 2012; Sequeiros *et al.*, 2018). Fig. 5i shows the bed shear velocity for the different cases. In general, the maximum value for u_τ is where $x_1 = 0$, followed by underflow's head and body, and the minimum value is observed upstream plunging. The magnitude of u_τ is function of the flow velocity, that in turn depends on the plunge point location, therefore, cases with the plunging upstream produce higher bed shear velocity u_τ. The animated versions of the flow visualization presented in Figs. 3, 4 and 5 are available as supplementary materials.

Fig. 6a shows the temporal evolution of the plunge point position x_p. Cases 2, 6 and 7 have the same flow discharge and increasing sediment concentration, which moves the plunge point upstream. Additionally, cases 4, 5 and 6 have the same sediment concentration and increasing flow discharge, which also moves the plunge downstream. Both parameters can be combined into the initial densimetric Froude number Fr_0, where a higher Fr_0 demands more distance for plunging and more runtime to eventually reach an asymptotic state. It is evident that for case 2, with highest initial Froude number, the plunge zone left the computational test section at around $t = 4,000$. Notice that the depth at plunge point is recovered by the linear equation $h_p = 1 + Sx_p$. Fig. 6b shows the temporal evolution of the front position x_f, while Fig. 6c shows the front velocity $u_f = dx_f/dt$, where a moving average in time is employed in order to smooth the signal. Notice that both curves are just defined while the front is inside the test section ($x_f \leq 250$). As discussed previously, the front velocity is strongly affected by the plunge point position, once it impulses the underflow's body and head. In this way, a higher front velocity is observed according to the same parameters that move the plunge point upstream, i.e., lower initial densimetric Froude number Fr_0, lower initial flow discharge Q_0 or higher initial sediment concentration C_0. Finally, Fig. 6d shows the time evolution of the densimetric Froude number at plunge position Fr_p, where a convergence to $Fr_p = 0.45$ is noticeable, in good agreement with previous studies (Parker and Toniolo, 2007; Lamb *et al.*, 2010; Schuch *et al.*, 2018). The averaged Froude number at plunge point measured is $Fr_p = 0.438 \pm 0.027$, taking an average in time ($4,000 \leq t \leq 6,000$) and between cases (excluding case 2, that left the computational test section). This value depends on the bed roughness, suspended grain size and bed slope, according to Sequeiros (2012). Besides, Fr_p can be useful in the development of new methodologies for the prediction of depth for plunging, or plunging criteria (Schuch, 2020; Schuch
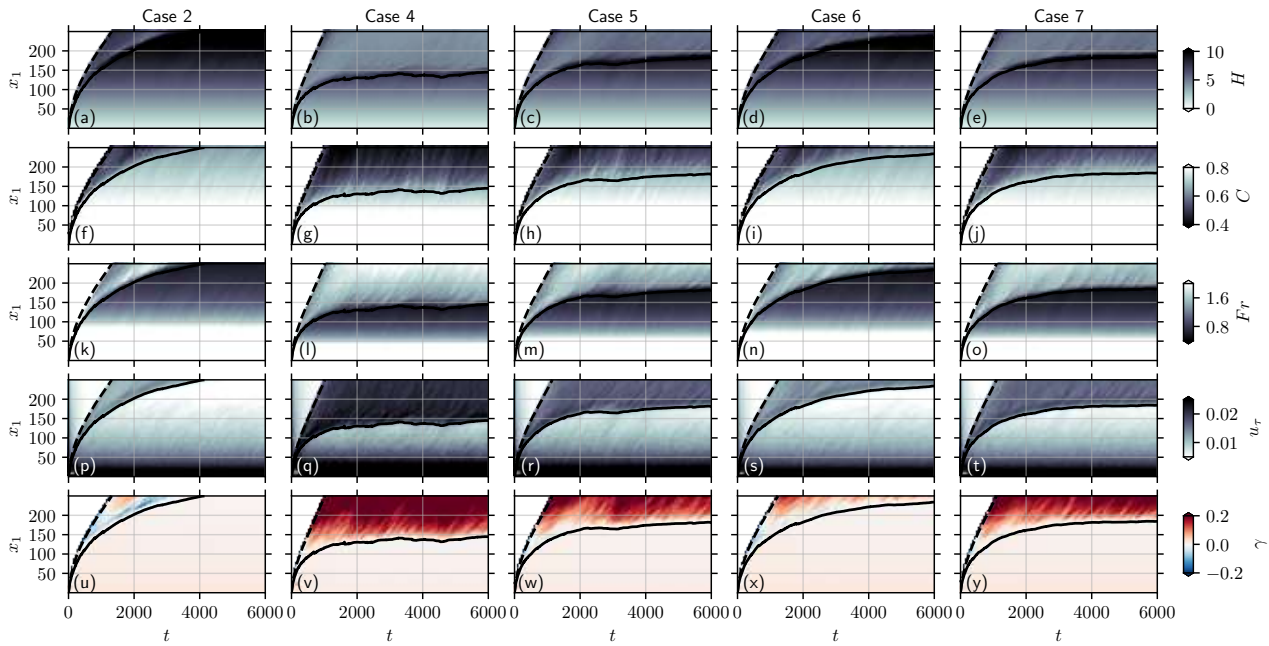
Figure 7. Spatio-temporal evolution of: Flow depth H, layer-averaged concentration C, densimetric Froude number Fr, spanwise-averaged bed shear velocity u_τ and mixing coefficient, from top to bottom, respectively. Cases 2, 4, 5, 6 and 7 are arranged from left to right. Plunging point x_p (solid lines) and front x_f (dashed lines) positions are shown for reference. Horizontal and vertical axis represent time t and stream-wise coordinate x_1, respectively.

et al., In prep).

Figure 7 shows the flow quantities under investigation as function of time t and the streamwise coordinate x_1, are they: Flow depth H, layer-averaged concentration C and densimetric Froude number Fr, computed according to Eq. (4), in addition to the mixing coefficient $\gamma = Q/Q_0 - 1$ and the bed shear velocity u_τ (5), from top to bottom, respectively. The positions for plunge point x_p (solid lines) and front x_f (dashed lines) are presented for reference. The five simulated cases are arranged horizontally. The entire spatio-temporal evolution is shown, where some topics discussed previously in Figs. 4 and 5 are visible in details. The maximum flow depth H (Fig 7a-e) occurs at plunge point, where the flow collapses and accelerates. The plunge point for case 2 left the test section (where $x_1 = 250$), its high initial Froude number demands a deeper domain in order to have a stable plunging position. The concentration C (Fig 7f-j) decays due to sedimentation, and the mixing with the ambient fluid downstream plunging is other process that reduces sediment concentration. The densimetric Froude number Fr (Fig 7f-j) decreases with the streamwise coordinate x_1, because the flow depth increases, until the minimum value at plunge zone. The acceleration at plunge zone increases Fr downstream plunging, as well as the increase in flow discharge due to entrainment. The densimetric Froude number measured downstream plunging Fr_d (at the end of the test section, where $x_1 = 250$) is equal to 1.93 ± 0.043, 1.722 ± 0.044, 1.385 ± 0.113 and 1.648 ± 0.047 for cases 4 to 7, respectively, all greater than one (e.g., supercritical), which is expected once the head has passed away in bed slopes steeper than about 1% according to Sequeiros (2012). Fig. 7p-t show the spanwise-averaged bed shear velocity u_τ, the highest value is observed for case 4 (Fig. 7q), with the shortest distance for plunging and higher underflow velocity. Fig. 7u-y show the mixing coefficient $\gamma = Q/Q_0 - 1$, that represents the increasing in the submerged flow discharge due to entrainment of ambient fluid into the turbidity current. Cases that have plunged early present more distance for entrainment, so the highest value is observed for case 4 (Fig. 7v), followed by case 7 (Fig. 7y) and case 5 (Fig. 7w). The plunging point for case 2 (Fig. 7u) left the computational test section, so the mixing coefficient is negligible for $t > 4,000$. On the other hand, this case has a negative mixing value (blue color) downstream plunging during the transient phase ($t < 4000$), indicating that the submerged turbidity current loses its volume to the ambient in a detrainment process. Notice that a pulsing phenomenon is observed for all cases, even though the variables are evaluated in a spanwise-averaged context and the input flow is kept steady, this phenomenon is investigated in details in Best *et al.* (2005) and Kostaschuk *et al.* (2018).

4. CONCLUSIONS

Numerical simulations play an essential role in many different research fields, since they can provide information on all variables for any point of time and space. Lab experiments are very often not able to provide such information, with data only available in a plane and/or locally. In this study, a new data-set is presented, covering the entire spatio-temporal

evolution of the plunge phenomenon and all quantities related to it using the layer-averaged context. Such database can be used to analyze the parameters and mechanisms that govern the flow transition in the plunge zone and support future research, it is available at https://github.com/fschuch/the-plunging-flow-by-3D-LES.

5. ACKNOWLEDGEMENTS

6. REFERENCES

Akiyama, J. and Stefan, H.G., 1984. "Plunging Flow into a Reservoir: Theory". *Journal of Hydraulic Engineering*, Vol. 110, No. 4, pp. 484–499. ISSN 0733-9429. doi:10.1061/(ASCE)0733-9429(1984)110:4(484).

Arita, M. and Nakai, M., 2008. "Plunging conditions of two-dimensional negative buoyant surface jets released on a sloping bottom". *Journal of hydraulic research*, Vol. 46, No. 3, pp. 301–306.

Bartholomew, P., Deskos, G., Frantz, R.A., Schuch, F.N., Lamballais, E. and Laizet, S., 2020. "Xcompact3d: An open-source framework for solving turbulence problems on a cartesian mesh". *SoftwareX*, Vol. 12, p. 100550.

Best, J.L., Kostaschuk, R.A., Peakall, J., Villard, P.V. and Franklin, M., 2005. "Whole flow field dynamics and velocity pulsing within natural sediment-laden underflows". *Geology*, Vol. 33, No. 10, pp. 765–768.

Chamoun, S., De Cesare, G. and Schleiss, A.J., 2016. "Managing reservoir sedimentation by venting turbidity currents: A review". *International Journal of Sediment Research*, Vol. 31, No. 3, pp. 195–204.

Dai, A., Cantero, M.I. and García, M.H., 2007. "Plunging of two-dimensional gravity currents". *Proc., 5th Int. Symp. on Environmental Hydraulics, IAHR, Temp, Ariz.*

Dai, A. and García, M.H., 2009. "Discussion of "note on the analysis of plunging of density flows" by gary parker and horacio toniolo". *Journal of Hydraulic Engineering*, Vol. 135, No. 6, pp. 532–533.

Dairay, T., Lamballais, E., Laizet, S. and Vassilicos, J.C., 2017. "Numerical dissipation vs. subgrid-scale modelling for large eddy simulation". *Journal of Computational Physics*, Vol. 337, pp. 252–274.

Ellison, T. and Turner, J., 1959. "Turbulent entrainment in stratified flows". *Journal of Fluid Mechanics*, Vol. 6, No. 3, pp. 423–448.

Farrell, G. and Stefan, H., 1986. "Buoyancy induced plunging flow into reservoirs and coastal regions, project report, no. 241, st". *Anthony Falls Hydr. Lab., University of Minnesota*.

Ford, D.E. and Johnson, M.C., 1981. "Field observations of density currents in impoundments". In *Surface water impoundments*. ASCE, pp. 1239–1248.

García, M., 1996. *Hidrodinamica ambiental*. Colección Ciencia y técnica. Universidad Nacional del Litoral.

Gautier, R., Laizet, S. and Lamballais, E., 2014. "A DNS study of jet control with microjets using an immersed boundary method". *International Journal of Computational Fluid Dynamics*, Vol. 28, No. 6-10, pp. 393–410.

Grinstein, F.F., Margolin, L.G. and Rider, W.J., 2007. *Implicit large eddy simulation: computing turbulent fluid dynamics*. Cambridge university press.

Horner-Devine, A.R., Hetland, R.D. and MacDonald, D.G., 2015. "Mixing and Transport in Coastal River Plumes". *Annual Review of Fluid Mechanics*, , No. September 2014, pp. 569–594.

Julien, P.Y., 1998. *Erosion and sedimentation*. Cambridge University Press, Cambrige, Reino Unido.

Kassem, A. and Imran, J., 2001. "Simulation of turbid underflows generated by the plunging of a river". *Geology*, Vol. 29, No. 7, pp. 655–658.

Kostaschuk, R., Nasr-Azadani, M.M., Meiburg, E., Wei, T., Chen, Z., Negretti, M.E., Best, J., Peakall, J. and Parsons, D.R., 2018. "On the causes of pulsing in continuous turbidity currents". *Journal of Geophysical Research: Earth Surface*, Vol. 123, No. 11, pp. 2827–2843.

Laizet, S. and Lamballais, E., 2009. "High-order compact schemes for incompressible flows: A simple and efficient method with quasi-spectral accuracy". *Journal of Computational Physics*, Vol. 228, No. 16, pp. 5989–6015.

Laizet, S. and Li, N., 2011. "Incompact3d: A powerful tool to tackle turbulence problems with up to $O(10^5)$ computational cores". *International Journal for Numerical Methods in Fluids*, Vol. 67, No. 11, pp. 1735–1757.

Lamb, M.P., McElroy, B., Kopriva, B., Shaw, J. and Mohrig, D., 2010. "Linking river-flood dynamics to hyperpycnal-plume deposits: Experiments, theory, and geological implications". *Geological Society of America Bulletin*, Vol. 122, No. 9-10, pp. 1389–1400.

Lamb, M.P. and Mohrig, D., 2009. "Do hyperpycnal-flow deposits record river-flood dynamics?" *Geology*, Vol. 37, No. 12, pp. 1067–1070.

Lamballais, E., Fortuné, V. and Laizet, S., 2011. "Straightforward high-order numerical dissipation via the viscous term for direct and large eddy simulation". *Journal of Computational Physics*, Vol. 230, No. 9, pp. 3270–3275.

Meiburg, E. and Kneller, B., 2010. "Turbidity currents and their deposits". *Annual Review of Fluid Mechanics*, Vol. 42, pp. 135–156.

Mulder, T., Syvitski, J.P.M., Migeon, S., Faugeres, J.C. and Savoye, B., 2003. "Marine hyperpycnal flows: initiation, behavior and related deposits. A review". *Marine and Petroleum Geology*, Vol. 20, No. 6, pp. 861–882.

Nasr-Azadani, M., Hall, B. and Meiburg, E., 2013. "Polydisperse turbidity currents propagating over complex topography: comparison of experimental and depth-resolved simulation results". *Computers & Geosciences*, Vol. 53, pp. 141–153.

Necker, F., Härtel, C., Kleiser, L. and Meiburg, E., 2002. "High-resolution simulations of particle-driven gravity currents". *International Journal of Multiphase Flow*, Vol. 28, No. 2, pp. 279–300.

Parker, G. and Toniolo, H., 2007. "Note on the analysis of plunging of density flows". *Journal of Hydraulic Engineering*.

Sagaut, P., 2006. *Large eddy simulation for incompressible flows: an introduction*. Springer Science & Business Media.

Schuch, F.N., Meiburg, E. and Silvestrini, J.H., In prep. "Plunging condition for particle-laden flows over sloping bottoms: three-dimensional turbulence-resolving simulations". In preparation for Computers & Geosciences.

Schuch, F.N., Pinto, L.C., Silvestrini, J.H. and Laizet, S., 2018. "Three-dimensional turbulence-resolving simulations of the plunge phenomenon in a tilted channel". *Journal of Geophysical Research: Oceans*, Vol. 123, pp. 1–13.

Schuch, F.N., 2020. *Análise do Mergulho de Escoamentos Hiperpicnais em Canal Inclinado por Meio de Simulação Numérica de Grandes Escalas*. Ph.D. thesis, Programa de Pós-Graduação em Engenharia e Tecnologia de Materiais. Escola Politécnica, PUCRS.

Sequeiros, O.E., 2012. "Estimating turbidity current conditions from channel morphology: A froude number approach". *Journal of Geophysical Research: Oceans*, Vol. 117, No. C4.

Sequeiros, O.E., Mosquera, R. and Pedocchi, F., 2018. "Internal structure of a self-accelerating turbidity current". *Journal of Geophysical Research: Oceans*, Vol. 123, No. 9, pp. 6260–6276.

Singh, B. and Shah, C., 1971. "Plunging phenomenon of density currents in reservoirs". *La Houille Blanche*, , No. 1, pp. 59–64.

Wunderlich, W.O. and Elder, R.A., 1973. "Mechanics of flow through man-made lakes". *Washington DC American Geophysical Union Geophysical Monograph Series*, Vol. 17, pp. 300–310.

7. RESPONSIBILITY NOTICE

The authors are the only responsible for the printed material included in this paper.